International Journal of Nanomedicine

Dovepress

open access to scientific and medical research

Open Access Full Text Article

ORIGINAL RESEARCH

DHTPY-Cu@ZOL-Enhanced Photodynamic Therapy: A Strategic Platform for Advanced Treatment of Drug-Resistant Bacterial Wound Infections

Biao Hou[1–3,*], Bo Li[4,*], Wanjun Deng[3,*], Bo Li[1,2], Bibo Ren[5], Chao Hu[3], Guowei Zhang[1,2], Fen Yang[6], Meimei Xiao[3], Songlin Xie[3], Denghui Xie[1,2]

[1]Department of Joint Surgery and Sports Medicine, Center for Orthopedic Surgery, Orthopedic Hospital of Guangdong Province, The Third Affiliated Hospital of Southern Medical University, Guangzhou, People's Republic of China; [2]Guangdong Provincial Key Laboratory of Bone and Joint Degeneration Diseases, Academy of Orthopedics, Guangzhou, Guangdong Province, People's Republic of China; [3]Department of Hand and Foot Microsurgery, The affiliated Nanhua Hospital, Hengyang Medical College, University of South China, Hengyang, People's Republic of China; [4]Department of Radiology, West China Hospital, Sichuan University, Chengdu, People's Republic of China; [5]College of Biomass Science and Engineering, Sichuan University, Chengdu, People's Republic of China; [6]Department of Infectious Diseases, The Affiliated Nanhua Hospital, Hengyang Medical College, University of South China, Hengyang, Hunan, People's Republic of China

*These authors contributed equally to this work

Correspondence: Denghui Xie; Songlin Xie, Email smuspine@163.com; xiesonglin0929@163.com

Purpose: This research was to innovate a nanozyme-based therapeutic strategy that combines aggregation-induced emission (AIE) photosensitizers with copper nanozymes. This approach is designed to address the hypoxic conditions often found in bacterial infections and aims to boost the effectiveness of photodynamic therapy (PDT) by ensuring sufficient oxygen supply for reactive oxygen species (ROS) generation.

Methods: Our approach involved the synthesis of dihydroxyl triphenyl vinyl pyridine (DHTPY)-Cu@zoledronic acid (ZOL) nanozyme particles. We initially synthesized DHTPY and then combined it with copper nanozymes to form the DHTPY-Cu@ZOL composite. The nanozyme's size, morphology, and chemical properties were characterized using various techniques, including dynamic light scattering, transmission electron microscopy, and X-ray photoelectron spectroscopy. We conducted a series of in vitro and in vivo tests to evaluate the photodynamic, antibacterial, and wound-healing properties of the DHTPY-Cu@ZOL nanozymes, including their oxygen-generation capacity, ROS production, and antibacterial efficacy against methicillin-resistant Staphylococcus aureus (MRSA).

Results: The DHTPY-Cu@ZOL exhibited proficient H_2O_2 scavenging and oxygen generation, crucial for enhancing PDT in oxygen-deprived infection environments. Our in vitro analysis revealed a notable antibacterial effect against MRSA, suggesting the nanozymes' potential to disrupt bacterial cell membranes. Further, in vivo studies using a diabetic rat model with MRSA-infected wounds showed that DHTPY-Cu@ZOL markedly improved wound healing and reduced bacterial presence, underscoring its efficacy as a non-antibiotic approach for chronic infections.

Conclusion: Our study suggests that DHTPY-Cu@ZOL is a highly promising approach for combating antibiotic-resistant microbial pathogens and biofilms. The biocompatibility and stability of these nanozyme particles, coupled with their improved PDT efficacy position them as a promising candidate for clinical applications.

Keywords: copper nanozyme, aggregate induced emission, photodynamic antibacterial therapy, antimicrobial resistance, diabetic wound healing

Introduction

The emergence of drug-resistant bacterial infections has become a significant public health challenge, particularly in relation to biofilm-associated antibiotic resistance.[1] Among these resistant bacteria, MRSA is notably prevalent in

Received: 19 April 2024
Accepted: 16 June 2024
Published: 21 June 2024

postoperative infections, non-healing ulcers, and burn infections.[2] Biofilms, as multicellular communities, are encapsulated within mechanically stable extracellular polymeric substances, creating specific microenvironments characterized by acidic or hypoxic conditions, along with oxidative stress.[3,4] These features render biofilms formidable physical and metabolic barriers, effectively protecting bacteria from antibiotics and immune system attacks.[5,6] The current clinical strategy for treating biofilms involves surgical debridement followed by systemic antibiotic therapy. However, prolonged antibiotic use may lead to increased resistance and potential organ toxicity.[7] Thus, there is an urgent need for new non-antibiotic strategies to combat biofilm-associated infections, especially those involving drug-resistant strains.

PDT has emerged as an innovative antimicrobial strategy owing to its precise spatiotemporal controllability, high efficiency, and non-invasiveness.[8] PDT employs a combination of photosensitizers, light, and molecular oxygen to generate ROS, including singlet oxygen ($^1O_2$), superoxide anion radicals ($O_2^{\cdot-}$), hydrogen peroxide (H_2O_2), and potent oxidizing hydroxyl radicals (OH).[9] Since PDT directly targets bacterial membranes, it is challenging for bacteria to develop resistance against this method.[10] However, traditional photosensitizers, such as ACQ-type photosensitizers, have limitations, including fluorescence quenching and reduced photodynamic activity, resulting from aggregation in aqueous solutions.[11] This has led to the exploration of new types of photosensitizers, particularly AIE-type photosensitizers, which exhibit enhanced optical activity and stability in aggregated states, overcoming the drawbacks of aggregation-caused quenching type photosensitizers.[12] AIE photosensitizers are a class of luminescent materials that display weak or no emission when molecularly dissolved but become highly emissive upon aggregation.[2] This unique phenomenon arises from the restriction of intramolecular motions (RIM) in the aggregated state, which suppresses non-radiative decay channels and enhances radiative emission.[13] AIE photosensitizers have garnered significant attention in recent years due to their superior photophysical properties, such as high quantum yields, excellent photostability, and large Stokes shifts.[14] These characteristics make AIE photosensitizers promising candidates for various biomedical applications, including photodynamic therapy.[15]

Nevertheless, the clinical application of PDT faces limitations due to its oxygen dependency, especially in infectious environments with low oxygen concentrations, significantly reducing the bactericidal efficiency of PDT.[16] To address this issue, various solutions have been proposed, including the use of oxygen carriers, enhancing tissue oxygen permeability, and developing new photosensitizers effective in hypoxic conditions.[17–19] However, these approaches have their limitations, such as complex preparation processes for oxygen carriers and challenges in chemical stability and biological distribution for new photosensitizers. With the rapid advancement of nanotechnology, nanozymes mimicking natural enzyme activities have become a research hotspot in the field of biomedicine.[20] Particularly, nanozymes with catalase (CAT)-like activity have garnered widespread attention due to their unique biochemical properties and broad application prospects.[21] These nanozymes can mimic the function of natural catalase, effectively catalyzing the decomposition of H_2O_2 into water and oxygen, thus playing a crucial role within the body.[22] Various types of nanozymes have been developed, including iron-based, manganese-based, and copper-based metal oxide nanozymes.[23,24] Each type of nanozyme has its unique properties and advantages, but the selection of a suitable nanozyme requires consideration of factors such as catalytic efficiency, biocompatibility, and stability.[25]

Among these nanozymes, copper nanozymes have attracted attention due to their high catalytic activity and good biocompatibility.[26] Copper nanozymes not only efficiently decompose H_2O_2 to produce oxygen but also exhibit outstanding performance in various biomedical applications due to their unique chemical properties.[27] For instance, in the field of tumor therapy, copper nanozymes have been used to alleviate tumor hypoxia, thereby enhancing the effectiveness of PDT.[28,29] Additionally, the choice of copper nanozymes is also based on their excellent chemical stability and tunable biological activity. Compared to other types of nanozymes, copper nanozymes exhibit higher stability within the body, which is crucial for long-term biomedical applications.[30] Furthermore, the surface of copper nanozymes can be chemically modified for functionalization, achieving specific biological effects such as targeted delivery, imaging, and therapy.[31,32] Therefore, copper nanozymes not only play a significant role in tumor therapy but also show great potential in antimicrobial, anti-inflammatory, and wound healing applications.[33,34]

In this context, our study proposes an innovative solution: utilizing nanozymes to generate oxygen at the site of bacterial infection, thereby overcoming the hypoxic limitations of PDT and enhancing its antimicrobial effectiveness, as well as alleviating the inflammatory reactions in the wound microenvironment. We have developed a novel AIE-type photosensitizer that, upon dissolution in water, assembles with other materials to form DHTPY-Cu@ZOL nanozyme particles. These nanozyme particles can generate O_2 in high H_2O_2 infection microenvironments, thereby mitigating biofilm hypoxia. The

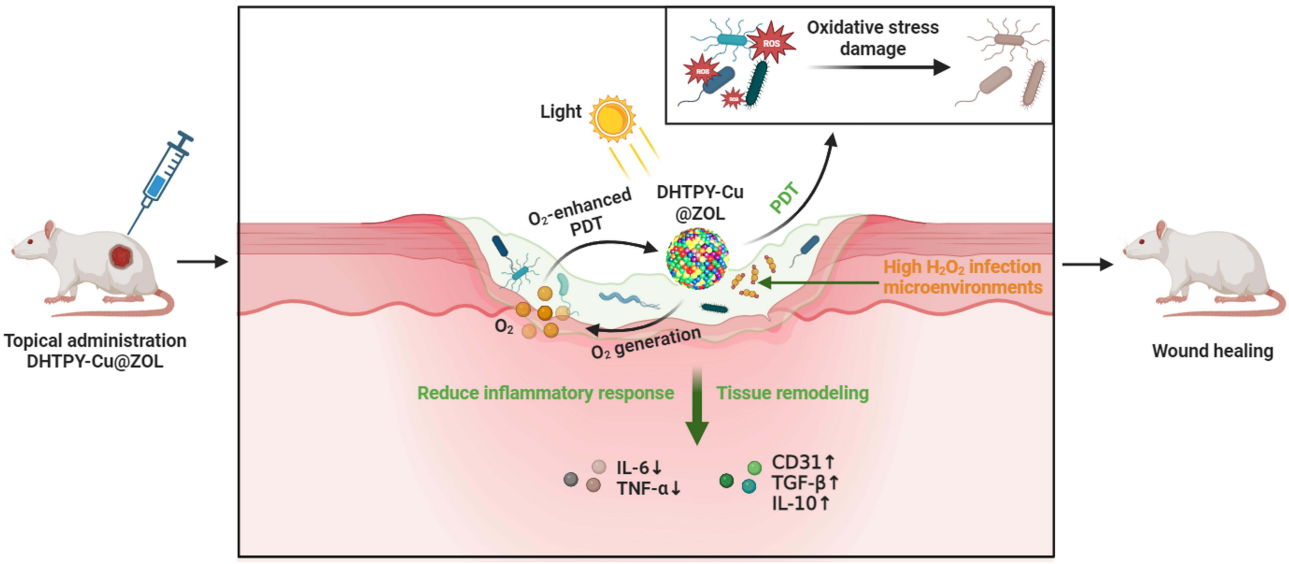

Scheme 1 Schematic illustration of the mechanism about oxygen-enhanced PDT mediated by the DHTPY-Cu@ZOL targeting chronic infection models.

continuous supply of O_2 further elevates the level of $^1O_2$, facilitating effective antimicrobial action through O_2-enhanced PDT. DHTPY-Cu@ZOL not only improves chronic inflammatory conditions but also accelerates the healing process in chronic infections. Overall, this study presents a promising non-antibiotic strategy, enhancing the biocompatibility and application range of the photosensitizer and offering new insights into the design and synthesis of nanozymes, for combating chronic wound infections and accompanying inflammation caused by drug-resistant bacteria (Scheme 1).

Materials and Methods

Material

Chemical reagents including 4-methylpyridine, 3-chloropropane-1,2-diol, 4-(diphenylamino)benzaldehyde, and zoledronic acid (ZOL) were acquired from Tansoole. Streptozotocin (STZ) was sourced from Merck KGaA, Darmstadt, Germany. Isolation of MRSA was carried out using human clinical samples, with subsequent identification performed at the Clinical Microbiology Laboratory of Nanhua Hospital, affiliated with Hengyang Medical College, University of South China, Hengyang, China. HaCaT keratinocytes were provided by the Chinese Academy of Sciences (Shanghai, China). HaCaT keratinocytes were cultured in an atmosphere with 5% CO_2 at 37°C in RPMI medium 1640 containing 10% FBS, 100 μg/mL streptomycin and 100 μg/mL penicillin. Human Umbilical Vein Endothelial Cells (HUVECs) were purchased from the American Type Culture Collection (ATCC). HUVECs were cultured in high-glucose Dulbecco's Modified Eagle's Medium (DMEM, Hyclone, USA) supplemented with 10% fetal bovine serum (FBS, Hyclone, USA) in culture incubators at 37°C with 5% CO2. Male Sprague–Dawley rats for experimental purposes were obtained from the University of South China's Animal Centre, located in Hengyang, China. Other solvents and reagents used in this study, all of analytical grade, were procured from various commercial supplier.

Synthesis of DHTPY

In this synthesis process, a combination of 4-methylpyridine (5.0 g, 54 mmol) and 2.3-dihydroxy-1-chloropropane (5.0 g, 45 mmol), both freshly distilled, was subjected to heating at 110°C for a duration of 48 h. The setup was shielded from moisture exposure using a calcium chloride drying tube. Upon cooling, the resultant solid formation was mechanically disrupted using a spatula. Subsequently, ethyl acetate (20 mL) was introduced to the mixture. The resultant solid was then isolated through filtration and further cleansed with ethyl acetate, leading to the acquisition of a moisture-sensitive, pale brown solid, hereafter referred to as "product a". For the next step, a reaction mixture containing 4-(diphenylamino)benzaldehyde (109 mg, 0.4 mmol) and product a (582 mg, 0.4 mmol) was prepared and subjected to reflux in dry ethanol, under an inert nitrogen atmosphere. This

reaction was catalyzed using a few drops of piperidine and allowed to proceed overnight. Post-cooling to ambient temperature, the solvent was eliminated via evaporation under reduced pressure. A neutral aluminum oxide column chromatography was using to purify the remaining residue, employing a dichloromethane and methanol mixture (40:1, v/v) as the eluent. This process yielded a red powder, identified as DHTPY.

Synthesis of Cu@ZOL

The Cu@ZOL nanocomposite was synthesized through a single-step assembly process. Initially, ZOL (10 mg) was uniformly dispersed in 1 mL of high-purity water with 10% Tris buffer (pH 8.8) and subsequently transferred into a reaction vessel upon complete dissolution. Next, a 50 μL aliquot of 0.1 M $CuSO_4$ aqueous solution was incrementally introduced into the mixture. The reaction proceeded for 2 h, after which the resultant product was isolated using a centrifugal filter unit (10 kDa Molecular Weight Cut-Off (MWCO)). This was followed by centrifugation at 5000 rpm (1740 × g) for 5 min and subsequent dual washes with ultrapure water, adjusting the final volume to 1 mL. Characterization of the Cu@ZOL composite involved dynamic light scattering, transmission electron microscopy (TEM), Fourier-transform infrared spectroscopy (FTIR), and ultraviolet (UV) spectroscopy.

Synthesis of DHTPY-Cu@ZOL Nanocomposite

The DHTPY-Cu@ZOL nanocomposite was synthesized via a streamlined one-pot approach. Initially, 10 mg of ZOL was uniformly suspended in 1 mL of high-purity water containing a 10% Tris buffer solution (pH 8.8). This mixture was then transferred into a reaction vessel after ZOL had completely dissolved. Subsequently, a 50 μL volume of 0.1 M $CuSO_4$ aqueous solution was gradually introduced into the mixture. The reaction was allowed to proceed for 2 h. Then, 30 μL of a 10 mM DHTPY solution was added to the post-reaction mixture. Afterward, the resultant composite was isolated in a centrifugal filter (10 kDa MWCO) and subjected to centrifugation at 5000 rpm (1740 × g) for 5 min. This step was followed by two rounds of washing with ultrapure water, after which the total volume was adjusted to 1 mL. The characterization of the synthesized DHTPY-Cu@ZOL involved techniques such as dynamic light scattering, TEM, UV spectroscopy, and X-ray photoelectron spectroscopy (XPS).

Characterization of DHTPY-Cu@ZOL

The size distribution and zeta potential of the various nanocomposites were quantified employing dynamic light scattering (DLS) with a ZEN 3600 Zetasizer (Malvern, UK). The structural morphology of the nanoparticles (NPs) was confirmed through TEM using a LIBRA 200 CS instrument (Carl Zeiss Co, Germany). Spectral data in the ultraviolet-visible (UV-vis) range were acquired using a HITACH UV–vis spectrophotometer (UH 5300, Japan). Additionally, the elemental makeup of the nanocomposites was elucidated via X-ray photoelectron spectroscopy (XPS) using a PHI 5400 model (PerkinElmer, USA).

Quantification of the DHTPY Concentration

The concentration of DHTPY was ascertained using UV spectroscopy. The procedure commenced with the preparation of a standard DHTPY solution. An accurately weighed amount of DHTPY was dissolved in water to create a stock solution with a concentration of 0.5 mM. Subsequently, a defined volume of this stock solution was transferred to a volumetric flask and further diluted with water. This step was repeated to generate a range of standard solutions with concentrations varying from 10 to 0.3 mM, specifically including 10, 5, 2.5, 1.25, 0.6125, and 0.3 mM. The absorbance of DHTPY at its characteristic UV absorption peak was measured using UV spectroscopy, and a standard curve was plotted. Finally, the samples were processed and tested.

$$\text{Loading Efficiency}\,(\%) = \text{Weight}_{\text{DHTPY}}/\text{Weight}_{\text{DHTPY-Cu@ZOL}} \times 100\%$$

Verification of the H_2O_2-Scavenging and O_2 Generation Assay Capability

At first, Cu@ZOL and DHTPY-Cu@ZOL at varying concentrations (0, 10, 25, 50, and 100 μg/mL) were used. Ammonium molybdate is utilized to detect the CAT enzyme mimetic activity of Cu@ZOL and DHTPY-Cu@ZOL

nanoparticles. The following control groups are established: Blank control group: 200 μL of H_2O; Negative control group: 50 μL of Cu@ZOL and DHTPY-Cu@ZOL (0, 10, 25, 50, and 100 μg/mL) + 50 μL of pure water + 100 μL of ammonium molybdate; Positive control group: 50 μL of H_2O_2 aqueous solution (100 mM) + 50 μL of H_2O + 100 μL of ammonium molybdate solution (100 mM). In the test group, 50 μL of Cu@ZOL and DHTPY-Cu@ZOL (0, 10, 25, 50, and 100 μg/mL) is incubated with 50 μL of H_2O_2 aqueous solution (100 mM) at room temperature for 1 minute. Then, 100 μL of ammonium molybdate solution (100 mM) is added. After 10 min, the absorbance at 405 nm was measured using an enzyme label instrument and recorded as A_{blank}, $A_{negative}$, $A_{positive}$, and A_{test}, respectively. The H_2O_2-scavenging capability was calculated from the following equation:

$$H_2O_2-\text{scavenging capability} = [(A_{positive}-A_{blank}) - (A_{test}-A_{negative})]/(A_{positive}-A_{blank}) \times 100\%$$

To compare with the natural CAT enzyme, we selected the most effective concentration of 100 μg/mL CAT enzyme, which was the same concentration as the nanoenzyme, to test the hydrogen peroxide scavenging rate. The test method used was identical to that employed for testing the nanoenzyme. Subsequently, we also tested the oxygen generation of the natural CAT enzyme, Cu@ZOL, and DHTPY-Cu@ZOL. The sample without enzyme was set as control group. Use a commercial oxygen meter (JPBJ-608 Portable Dissolved Oxygen Meter, Shanghai Ruiyi Instrument Factory) to record the real-time content of O_2 generated every 60 seconds.

Photodynamic Property of DHTPY-Cu@ZOL

1,3-Diphenylisobenzofuran (DPBF) was used as $^1O_2$-trapping agent to characterize the photodynamic property. To investigate the O_2-enhanced ROS generation by DHTPY-Cu@ZOL, the H_2O_2 solution (100 μM) was mixed into a DPBF solution (10 mM, 1 mL) as work solution. Then, DHTPY and DHTPY-Cu@ZOL were added to prepared work solution, respectively. After white light irradiation (40 mW/cm²) for different times, the absorbance spectra of collected supernatant were recorded with a UV–Vis spectrophotometer.

In vitro Cytotoxicity Assay

The cytotoxic effects of the Cu@ZOL and DHTPY-Cu@ZOL formulations (0–150 μg/mL) on HaCaT keratinocytes were assessed using the Cell Counting Kit-8 (CCK-8, Dojindo Laboratories, Japan) assay. In brief, cells were plated in 96-well plates at a density of 10^4 Colony-forming units (CFU) per well and incubated overnight at 37 °C. Following the manufacturer's protocol, CCK8 solution was then added to each well and the incubation continued for an additional hour. Cell viability was measured by recording the optical density at 450 nm (OD 450) using a Varioskan Flash microplate reader (ThermoFisher Scientific, USA). The results were expressed as the mean cell viability calculated from triplicate wells using the formula $[(OD_{treat} - OD_{blank})/(OD_{control} - OD_{blank}) \times 100\%]$.

In vitro Antibacterial Test

MRSA was cultured with nanocomposite, respectively, including Control (PBS), Cu@ZOL (100μg/mL), DHTPY-Cu@ZOL (100μg/mL). Briefly, 200 μL of bacterial suspension (1×10^7 CFU/mL) was added to the surface of each nanocomposite in a 48-well culture plate. After culture for 4 h, 800 μL of Luria-Bertani broth was added to each well to re-suspend the bacterial, and then the optical density (OD) of the bacterial suspension was measured at 600 nm after incubation for another 10 h at 37 °C. The antibacterial ratio of various nanocomposites was calculated from the following equation:

$$\text{Antibacterial ratio}\,(\%) = \left(OD_{control}-OD_{Sample}\right)/OD_{control} \times 100\%$$

The specific operational steps of the flat panel technique were as follows. First, the solid medium (60 °C) was added to petri-dish and cooled at room temperature to form a solid flat panel. Second, the bacterial resuspension of control group was diluted to 10^2 CFU/mL using PBS solution. Then, the bacterial suspensions of Cu@ZOL and DHTPY-Cu@ZOL were diluted using the same dilution factor as the blank group. Final, 100 μL diluted bacteria resuspension was coated to the surface of solid flat panel and cultured for 12 h in the shaking table.

Observation of the Live/Dead Staining of the Bacteria by CLSM

The bacteria were treated with DHTPY-Cu@ZOL (100μg/mL), and then further irradiated with white light irradiation (40 mW/cm²) for 10 min. A mixed SYTO9 and PI dyes (live/dead BacLight bacterial viability kit, Invitrogen, USA) were co-incubated with MRSA for 20 min. By observing in a confocal laser scanning microscope (CLSM, Leica Germany), live bacteria display green fluorescence, whereas dead bacteria with an impaired membrane structure mainly show red fluorescence.

Observation of ROS Accumulation in MRSA by Microplate Reader

ROS accumulation in MRSA was detected with the Reactive Oxygen Species Assay Kit (Beyotime, China) according to the reagent instructions. In brief, the bacteria grown overnight at 37 °C were washed and suspended in PBS to obtain an OD_{600} of 0.5. Bacterial suspensions were added with DCFH-DA at a final concentration of 10 μM and then incubated at 37 °C for 30 min. After washing the bacteria with PBS three times, 190 μL of probe-labeled bacterial suspensions and 10 μL PBS, DHTPY (14μg/mL), and DHTPY-Cu@ZOL (100μg/mL) were simultaneously added to the 96-well plates, and then 96-well plates were exposed to white light for 10 min, and the fluorescence intensities were immediately measured by a microplate reader at 488/525 nm.

Observation of the Bacterial Morphology in Bacteria by SEM

Bacteria in different groups were fixed with paraformaldehyde (4 wt %) at 4 °C for 6 h. After being washed with PBS for 3 times, fixed samples were serially dehydrated in an ethanol series (20%, 40%, 60%, 80%, and 100%) and tert-butyl alcohol, each for 15 min. Finally, the dehydrated samples were dried in a drier and coated with gold for SEM observation.

Observation of Biofilm Structure by CLSM

MRSA biofilms were cultivated in confocal microscopy dishes. Post various treatments, biofilms were stained with 500 μL of Syto9 (concentration: 5 μM) in a dark environment for a duration of 30 min. The architecture of these biofilms was then examined using a CLSM. To quantify the relative fluorescence intensity of the SYTO9 channel in the biofilms, five distinct imaging regions were analyzed utilizing the ImageJ/FIJI software, available at https://imagej.nih.gov/ij/.

Detection of Oxygen Content in Cell Culture Medium

To evaluate the capability of Cu@ZOL and DHTPY-Cu@ZOL to enhance oxygen content in the culture environment of HUVEC cells, cells were first seeded in standard cell culture plates and cultured at 37°C with 5% CO_2 until near log phase growth. Twenty-four hours after seeding, the medium was replaced with fresh culture medium containing Cu@ZOL and DHTPY-Cu@ZOL added at a concentration of 100 μg/mL with 3 parallel samples in each group. The control group received the same volume of medium without nanoparticles. All samples were incubated for 4 hours in a cell incubator, after which a portable dissolved oxygen meter was used to measure the oxygen concentration in the medium. Upon completion of the experiment, data were collected and analyzed to assess the impact of the different treatments on the oxygen environment around the HUVEC cells.

Characterizations of Cellular Migration and Tube Formation Assay in vitro

In vitro scratch assay: HUVECs were seeded at a density of 5×10^5 cells per well in 6-well plates. After culture for 24 h, a sterile pipette tip was used to scratch the cells, and unattached cells were removed by PBS washing. Then, fresh DMEM containing 2% serum was added, and the attached cells were treated with PBS, Cu@ZOL or DHTPY-Cu@ZOL, respectively. Cell migration was photographed and recorded using a microscope (Thermo Fisher, USA) at 0 h and 24 h, respectively. The distance between the edges of the scratch at different time points was analyzed using Image J software.

In vitro tube formation assay: 1000 μL of Matrigel (Growth factor reduced, BD, USA) was added to the 6-well plates and allowed to solidify at 37°C for 30 min. Then, HUVECs were seeded at a density of 5×10^5 cells. The plates were treated with PBS, Cu@ZOL or DHTPY-Cu@ZOL, respectively. After culture for 12 h, the formation of the tube stained with Calcein-AM (Beyotime, China) was captured with a microscope, and the tube length was analyzed by ImageJ software.

Evaluation of the Effect of DHTPY-Cu@ZOL on Infected Diabetic Wound Healing in vivo

Male SD rats weighing between 220 and 250 grams were administered 30 mg/kg of STZ daily for six days. Subsequently, their blood glucose levels were monitored using a Roche Diagnostics glucose meter (Shanghai, China). Rats exhibiting blood glucose levels exceeding 16.7 mmol/L for a week were classified as diabetic. In each diabetic rat, a 10 mm diameter full-thickness skin lesion was created and secured with a silicone ring to prevent contraction of the skin. To initiate infections, each diabetic wound was inoculated with 20 μL of a 1×10^7 CFU/mL MRSA solution. The wounds were then treated with different agents: PBS (Control group), Cu@ZOL and DHTPY-Cu@ZOL, each at a concentration of 100 μg/mL under white light irradiation (40 mW/cm²), consistent with the in vitro settings. Post-Light irradiation for 20 min, wounds were covered with a 3M Tegaderm™ film (3M Health Care, USA).

On the 9th and 14th day, wound tissues were harvested for histological examination. These tissues underwent fixation, dehydration, and paraffin embedding before being sectioned. Histological analyses, including Hematoxylin and Eosin (H&E) staining, Masson's trichrome staining, immunohistochemical staining, and immunofluorescence staining were performed on these sections to evaluate inflammatory infiltration, reepithelialization, collagen synthesis, and angiogenesis. The initial preparation of tissue sections involved overnight fixation in 4% paraformaldehyde, followed by sequential immersion in ethanol solutions of increasing concentrations (70%, 80%, 90%, 95%, and twice in 100% ethanol for 20 min each). Post-dehydration, the samples were cleared in xylene, embedded in paraffin, and sectioned (5–8 μm thick). Immunofluorescence staining was also carried out to determine anti-inflammatory efficacy using appropriate primary and secondary antibodies. The sections were first permeabilized with 0.1% Triton X-100 for 15 min, then blocked with 10% goat serum for one hour. They were incubated with primary antibodies overnight at 4°C, followed by secondary antibodies for 2 h at room temperature. Nuclei were counterstained with DAPI for 5 min, and the slides were imaged using CLSM.

Fourteenth day post-treatment, the bacterial load in the infected wounds was quantified using the spread plate technique. Tissue samples from the wound sites were collected, placed in sterile PBS, and homogenized. The homogenates were cultured on agar plates and incubated overnight at 37°C to enumerate bacteria. Additionally, homogenates were centrifuged (5000 × g, 4°C, 5 min), and the supernatants were used for ELISA to measure cytokine levels, including TGF-β and IL-6. These cytokines were quantified using the QuantiCyto ELISA Kit (Neobioscience technology) as per the manufacturer's guidelines.

Statistical Analysis

The statistical graph was drawn by GraphPad Prism 8.0 software (GraphPad Software, USA). Statistical analyses were performed using the SPSS software package (IBM SPSS software package 21.0). Data are presented as mean ± standard deviation (SD) and each datum was replicated at least 3 or more independent measurements. Data differences were assessed using one-way ANOVA or *t*-test, and *P < 0.05, **P < 0.01, and ***P < 0.001 were considered statistically significant, ns represented no significance.

Results and Discussions

Characterization of DHTPY@Cu-ZOL

First, we synthesized a dual hydroxy AIE photosensitizer. The modification with dual hydroxyl groups was aimed at enhancing the water solubility of the photosensitizer,[35] which theoretically allows for a higher loading rate, thereby augmenting the photodynamic effects of nanomaterials. The experimental procedures are broadly illustrated in Figure 1A and B. Subsequently, we tested the nuclear magnetic resonance (NMR) hydrogen spectrum of the product a ^{1}H NMR (600 MHz, Methanol-d_4) δ 8.80–8.74 (m, 2H), 7.93 (d, J = 6.3 Hz, 2H), 4.77 (dt, J = 13.3, 2.8 Hz, 1H), 4.52 (ddd, J = 13.4, 8.4, 1.3 Hz, 1H), 4.01 (tdd, J = 9.1, 4.7, 2.9 Hz, 1H), 3.67 (dd, J = 11.3, 4.8 Hz, 1H), 3.49 (ddd, J = 11.3, 6.2, 1.7 Hz, 1H), 2.69 (s, 3H), and DHTPY ^{1}H NMR (600 MHz, DMSO-d_6) δ 8.77 (d, J = 6.6 Hz, 2H), 8.33 (s, 1H), 8.21–8.14 (m, 2H), 7.96 (d, J = 16.2 Hz, 1H), 7.67–7.61 (m, 2H), 7.42–7.37 (m, 3H), 7.33 (d, J = 16.1 Hz, 1H), 7.20–7.11 (m, 5H), 7.00–6.93 (m, 2H), 5.47 (d, J = 5.5 Hz, 1H), 5.08 (t, J = 5.4 Hz, 1H), 4.65 (dd, J = 13.3, 3.1 Hz, 1H), 4.35 (dd, J = 13.2, 8.5 Hz, 1H), 3.91–3.85 (m, 1H), 3.51 (dt, J = 10.4, 5.0 Hz, 1H), 1.24 (s, 1H) (Figure 1C and D), confirming the successful synthesis of the photosensitizer.

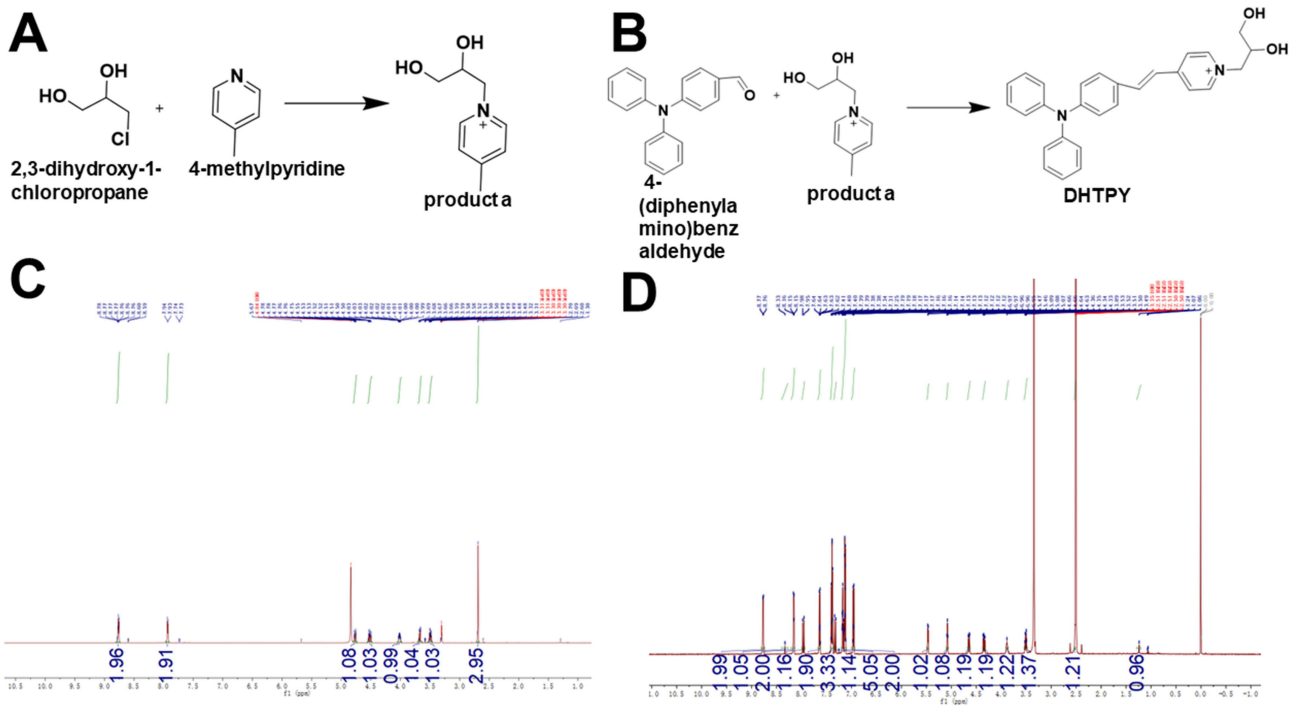

Figure 1 Synthesis scheme of (**A**) and (**B**) DHTPY photosensitizer and corresponding NMR spectra (**C** and **D**).

A primary objective in our material design was to combine the photosensitizer with copper nanoenzymes. Copper nanoenzymes typically exhibit robust redox activity, good biocompatibility, and lower toxicity, making them safer for biomedical applications.[31] Furthermore, copper is a relatively inexpensive and abundant material, potentially offering cost-effectiveness. Initially, literature indicated the use of alendronate with dual phosphate groups for chelating cerium ions to form nanoenzymes. There was also exploration into the possibility of chelating copper to form nanoenzymes, but without further validation. Thus, we began designing to ascertain whether copper ions chelated by alendronate with dual phosphate groups could form nanoenzymes demonstrating effective therapeutic outcomes in biological applications. To visually represent the ligand chelating copper ions, we created 3D molecular graphics (Scheme S1-S3). The intelligent molecule ZOL, which combines the high affinity of imidazole and dual phosphate groups for copper metal ions, was used to mediate the assembly of metal nanoenzymes. As shown in Figure 2A, ZOL self-assembled with copper ions and the photosensitizer to form DHTPY-Cu@ZOL, with an optimal feeding ratio selected based on literature research and preliminary experiments.[36] To test the loading rate of the photosensitizer, we conducted a standard UV curve analysis for the photosensitizer which was 14% (Figure S1A). Then, the release profile of DHTPY was measure for 7 days in PBS. The result clarifies that the photosensitizer used in our study exhibits high stability under normal PBS conditions (Figure S1B). The morphological characteristics of DHTPY-Cu@ZOL, characterized in Figure 2B, showed uniform spherical dispersion with an average size of about 10 nm. Further DLS analysis indicated a hydrated particle size of about 18 nm and a PDI of 0.114. The hydrated particle size is larger than the dry state size, as water in solution forms a hydration layer around the nanoparticles, which reduces in size during TEM sample preparation due to dehydration. We also measured its stability over 48 h, finding the nanoscale size to be stable, thus demonstrating the good stability of DHTPY-Cu@ZOL (Figure 2C and D). Then, we measured the potentials of Cu@ZOL and DHTPY-Cu@ZOL. Zeta potential measurements showed that, compared to Cu@ZOL, the surface of DHTPY-Cu@ZOL loaded with the photosensitizer remained negatively charged but decreased, possibly due to the positive charge of the pyridinium salt in DHTPY increasing its potential (Figure 2E). We then tested the UV characteristic peaks of Cu@ZOL and DHTPY-Cu@ZOL. DHTPY-Cu@ZOL showed characteristic peaks around 300 nm and 470 nm, where the peak around 300 nm is characteristic of Cu@ZOL and the peak near 470 nm is characteristic of the photosensitizer. All these structures indirectly evidenced the successful loading of the photosensitizer into the nanoenzyme (Figure 2F). The XPS spectrum of DHTPY-Cu@ZOL showed a single peak near 132.7eV from the splitting of the phosphorus 2P level originating from the ZOL ligand, and double peaks near 933.2eV and 952.8eV from the

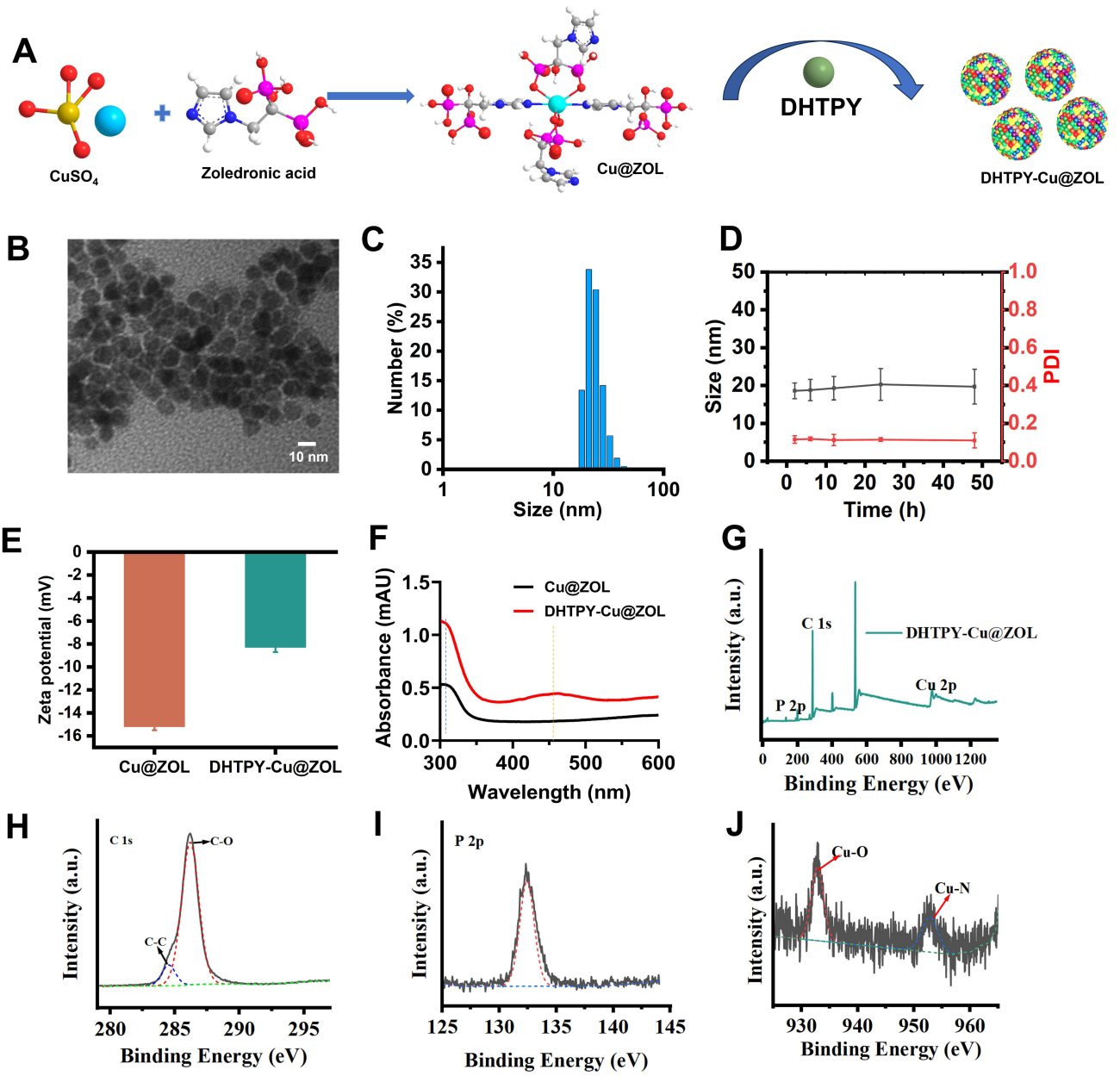

Figure 2 Characterization of DHTPY-Cu@ZOL. (**A**) Synthesis Scheme of DHTPY-Cu@ZOL. (**B**) Representative TEM image and. (**C**) Hydrodynamic particle size of DHTPY-Cu@ZOL. (**D**) The stability of DHTPY-Cu@ZOL. (**E**) The Zeta potential of Cu@ZOL and DHTPY-Cu@ZOL. (**F**) The ultraviolet absorption spectra of Cu@ZOL and DHTPY-Cu@ZOL. (**G**) The XPS of DHTPY-Cu@ZOL and its high resolution of (**H**) C 1s, (**I**) P 2p and (**J**) Cu 2p.

splitting of the copper 2p level. The peak strength of copper-oxygen was twice that of copper-nitrogen, indicating the successful chelation of the ZOL ligand with copper ions, and thereby verifying the previously mentioned theoretical chelation method of ZOL and Cu (Figure 2G–J). All these structures indicate that copper nanoenzymes can serve as a multifunctional platform for co-assembly with other drugs. Theoretically, drugs could be encapsulated within through π-π stacking interactions and hydrophobic forces, yet the precise mechanism of such co-assembly requires further investigation.[37]

H_2O_2 Scavenging, O_2-Supplying, and Photodynamic Properties of DHTPY-Cu@ZOL

Appropriate oxygen supply is one of the necessary conditions for achieving effective photodynamic effects.[38] One of the main purposes of designing DHTPY-Cu@ZOL is to alleviate the weakening of PDT due to high H_2O_2 and low oxygen in the microenvironment of bacterial infections. As shown in Figure 3A, DHTPY-Cu@ZOL generates O_2 in response to high H_2O_2. Then, under white light irradiation, the continuous supply of O_2 can further enhance the production of $^1O_2$ by

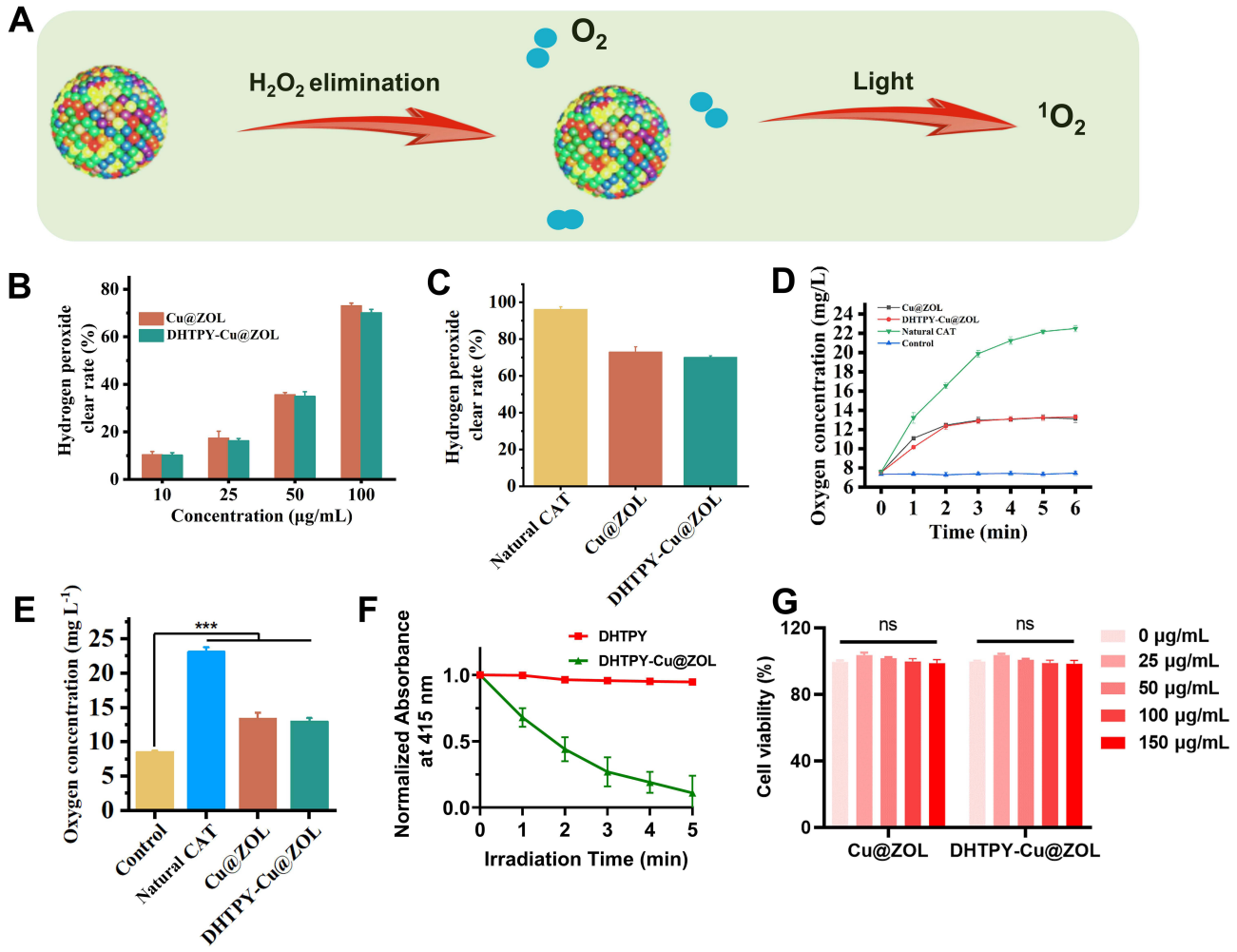

Figure 3 (**A**) Schematic illustration of the mechanism about the DHTPY-Cu@ZOL enhanced O_2 generation for PDT. (**B**) H_2O_2 scavenging behaviors after incubation Cu@ZOL, DHTPY-Cu@ZOL at mass concentration. (0, 25, 50, and 100 μg mL^{-1}) (n = 5). (**C**) H_2O_2 scavenging behaviors after incubation CAT, Cu@ZOL and DHTPY-Cu@ZOL (100 μg mL^{-1}) (n = 3). (**D**) The changes of dissolved O_2 level in H_2O_2 solution (100 μM) after co-incubation with Cu@ZOL and DHTPY-Cu@ZOL in different time (n = 3). (**E**) The changes of dissolved O_2 level in H_2O_2 solution (100 μM) after co-incubation with Cu@ZOL and DHTPY-Cu@ZOL in different time. (100 μg mL^{-1}) (n = 3, ***P < 0.001). (**F**) Irradiation of DHTPY and DHTPY-Cu@ZOL with white light in the presence of DPBF probe (100 μM H_2O_2), and their respective changes at 410 nm within 5 min post-irradiation (n = 3). (**G**) DHTPY-Cu@ZOL activity on HaCaT keratinocytes at various concentrations (0, 25, 50, 100 and 150 μg mL^{-1} (n=5, ns represented no significance).

DHTPY-Cu@ZOL. Thus, through this method, the elimination of bacteria at wound infection sites can be achieved via oxygen-enhanced PDT. The H_2O_2 scavenging ability was studied by quantifying the remaining H_2O_2, and it was observed that with increasing concentrations of Cu@ZOL and DHTPY-Cu@ZOL, the H_2O_2 scavenging ability gradually strengthened. DHTPY-Cu@ZOL at 100 μg/mL can significantly clear nearly 68% of H_2O_2 (Figure 3B and C). Under H_2O_2-rich conditions, DHTPY-Cu@ZOL and Cu@ZOL increased O_2 production over time, eventually reaching around 13 mg/mL (Figure 3D and E), demonstrating the CAT-like enzyme activity of DHTPY-Cu@ZOL. Cu@ZOL and DHTPY-Cu@ZOL can trigger satisfactory O_2 generation in different concentrations of 100 μM H_2O_2 solution, indicating the potential functionality of the nanoenzyme to increase ROS.

DPBF probe was used to assess the generation of $^1O_2$. Typically, DPBF has a characteristic absorption peak at 410 nm, which irreversibly diminishes in the presence of $^1O_2$. When DPBF was co-incubated with suspensions of DHTPY and DHTPY-Cu@ZOL containing 100 μM H_2O_2, the absorption at 410 nm of DHTPY-Cu@ZOL irradiated with white light gradually decreased, indicating the generation of $^1O_2$ (Figure 3F). However, irradiated DHTPY showed no significant change, suggesting that DHTPY alone has virtually no $^1O_2$ generation effect. This is because the dual hydroxy DHTPY is an AIE-type photosensitizer, which can be dissolved in aqueous solutions with dual hydroxy modifications, leading to the deactivation of the photosensitizer and thus producing only a small amount of reactive oxygen under light conditions.

Cytocompatibility Assay of Cu@ZOL and DHTPY-Cu@ZOL

To study the effective concentration of DHTPY-Cu@ZOL for further in vitro and in vivo biological experiments, the cytotoxicity of DHTPY-Cu@ZOL to HaCaT keratinocytes was investigated using the CCK-8 assay. It was observed that within the concentration range of 25 to 150 μg/mL, Cu@ZOL and DHTPY-Cu@ZOL are safe for HaCaT keratinocytes (Figure 3G). These results suggest that DHTPY-Cu@ZOL has good biocompatibility, laying a solid foundation for further in vivo experiments.

Antibacterial Performance of DHTPY-Cu@ZOL

$^1O_2$ generated by PDT is regarded as an antimicrobial molecule.[39] It functions by disrupting bacterial cell membranes, a mechanism that makes it difficult for bacteria to develop resistance against PDT. Owing to the CAT enzyme activity of DHTPY-Cu@ZOL, which can increase oxygen levels in infected wounds, it is theoretically that a rapid release a large amount of $^1O_2$ under light irradiation can occur. Consequently, DHTPY-Cu@ZOL may exhibit stronger antibacterial effects than compared to traditional PDT, while also alleviating H_2O_2 levels at the wound site, promoting wound healing. In evaluating the antibacterial effect of DHTPY-Cu@ZOL, MRSA was chosen as the test organism. CFU counts represent the survival rate of bacteria after various treatments. DHTPY-Cu@ZOL-mediated PDT (DHTPY-Cu@ZOL group) significantly inhibited the growth of MRSA (Figure 4A). In the anti-MRSA experiment, Cu@ZOL alone exhibited virtually no antibacterial effect (Figure 4B), as it only catalyzes the conversion of H_2O_2 to oxygen, which is

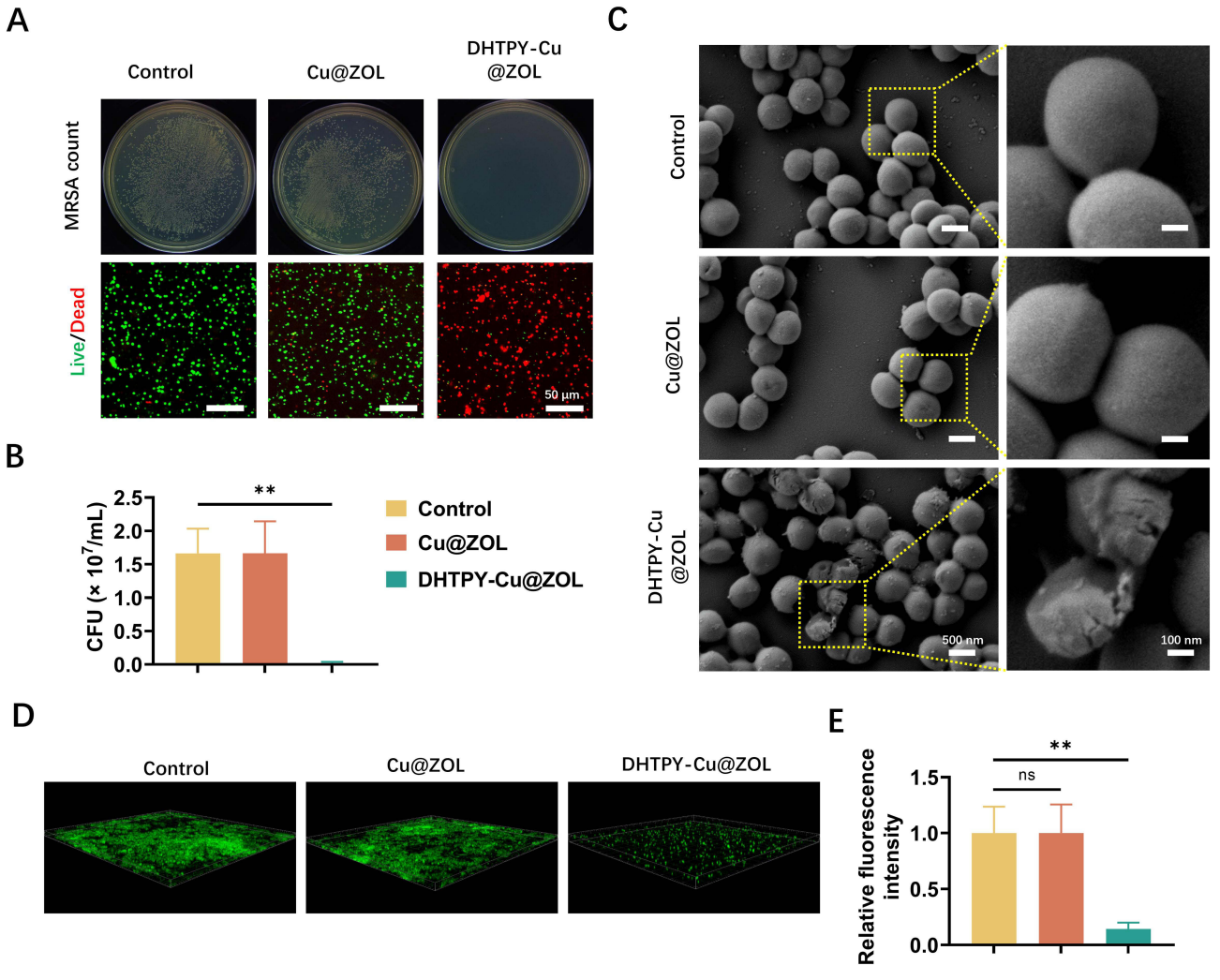

Figure 4 (**A**) Images of MRSA CFUs and live/dead staining images of MRSA after different treatments in vitro (n = 3). (**B**) Quantitative analysis of CFU from various treatment conditions in vitro (n =3). (**C**) Representative SEM micrographs of bacteria after different treatments. (**D**) 3D CLSM images of MRSA biofilms treated with different formulations (PBS, Cu@ZOL and DHTPY-Cu@ZOL with white light irradiation). (**E**) Relative fluorescence intensity of green staining in three groups of MRSA biofilms by ImageJ (n = 5, **P < 0.01, ns represented no significance).

non-toxic to bacteria. In our in vitro experiments, a group with only the DHTPY photosensitizer was not included, since DHTPY alone exhibits virtually no $^1O_2$ generation effect. This was verified in our previous material experiments, as the dual hydroxy DHTPY is an AIE-type photosensitizer that can dissolve in aqueous solutions due to the dual hydroxy modification, leading to the deactivation of the photosensitizer and thus producing only a small amount of reactive oxygen under light conditions, insufficient to disrupt bacterial cell membranes and exert an antibacterial effect.

Furthermore, live and dead bacteria were observed via CLSM following PI and SYTO staining (Figure 4A). The trend of bacterial killing was consistent with the bacterial survival rate obtained from CFU counts, proving the highly efficient antibacterial capability of DHTPY-Cu@ZOL (Figure 4B). ROS accumulation in the bacteria was measured as shown in Figure S4, the intensities of fluorescence emitted from DCFH-loaded bacteria increased following the addition of DHTPY, or DHTPY-Cu@ZOL. The fluorescence density of DHTPY-Cu@ZOL group was much higher than that in DHTPY group, highlighting that ensuring sufficient oxygen supply for reactive oxygen species (ROS) generation boosted the effectiveness of PDT. To elucidate the antibacterial mechanism of DHTPY-Cu@ZOL, SEM was employed to examine the morphological changes and membrane integrity of MRSA (Figure 4C). Compared to the control treatment, post-DHTPY-Cu@ZOL treatment showed reduced membrane integrity, with more shrinkage and rupture. The shape of MRSA no longer remained spherical, and cellular contents began to leak. This phenomenon is consistent with the mechanism of photodynamic antibacterial action. These results all validate the efficient antibacterial capability of DHTPY-Cu@ZOL, suggesting that CAT copper nanoenzyme-mediated PDT might be a more efficient antibacterial strategy. The antibacterial efficacy of DHTPY-Cu@ZOL against biofilm formation was evaluated, and the biofilms were quantitatively analyzed post-staining with crystal violet. As depicted in Figure 4D and E, the control groups demonstrated a notably higher density of biofilms. Conversely, the application of Cu@ZOL combined with white light exposure did not exhibit significant anti-biofilm activity. However, a marked reduction in biofilm formation, by approximately 85.6%, was observed in samples treated with DHTPY-Cu@ZOL under white light irradiation, underscoring its potent anti-biofilm properties.

Therapeutic Effect of DHTPY-Cu@ZOL on HUVECs Migration and Angiogenesis

Our experimental findings demonstrate a notable increase in both intra- and extracellular oxygen levels upon treatment with Cu@ZOL and DHTPY-Cu@ZOL, as reflected in the oxygen measurements obtained from the cell culture media (Figure S5). The ability of these nanoparticles to elevate oxygen levels could be particularly beneficial in overcoming the hypoxic conditions often encountered in wound environments, which typically hinder the efficacy of therapeutic interventions. We examined the effect of DHTPY-Cu@ZOL accelerated cell migration via scratch assay. As shown in Figure S6A and S6B, addition of Cu@ZOL and DHTPY-Cu@ZOL boosted the migration of HUVECs and expedited the closure of cell-free gaps compared to the control group, suggesting that both Cu@ZOL and DHTPY-Cu@ZOL have the ability to promote cell migration. Using a Matrigel tube formation assay, we next evaluated the angiogenesis capability of HUVECs treated in different groups (Figure S7A and S7B). Results showed that the total tube length assessed after 24 h in Cu@ZOL and DHTPY-Cu@ZOL groups was significantly higher than in the control group. These results suggested that Cu@ZOL promoted angiogenesis, which was comparable to DHTPY-Cu@ZOL.

Therapeutic Effect of DHTPY-Cu@ZOL on Diabetic Infected Wound Healing

To investigate the in vivo therapeutic effect of DHTPY-Cu@ZOL in PDT, a MRSA-infected diabetic rat wound model was established, simulating clinically observed infected diabetic skin ulcers. Blood glucose levels of the treated rats were measured, and those with consistent levels not exceeding 17.2 mM were selected. In preliminary in vivo studies, Cu@ZOL and DHTPY-Cu@ZOL (100 μg/mL) were applied on the 0th and 3rd days, respectively (Figure 5A). In this study, a full-thickness skin defect wound of 10 mm diameter was created using a circular skin biopsy punch on rats. On the 14th day in the control group, the skin wounds showed swelling and pus formation, typical symptoms of bacterial infection (Figure 5B). Both Cu@ZOL and DHTPY-Cu@ZOL exhibited certain wound healing effects post-irradiation in vivo. We hypothesize that the therapeutic effect of Cu@ZOL alone is due to the characteristics of chronic diabetic wounds, which are high blood sugar and a pro-inflammatory environment, leading to excessive accumulation of H_2O_2 at the injury site. This accumulation can cause severe inflammatory responses and hinder the tissue regeneration process. Cu@ZOL reduced the H_2O_2 concentration at the infection site and generated oxygen, which, according to the literature, has a positive therapeutic effect on chronic infected wounds.[40] On the 14th day, the DHTPY-Cu@ZOL group showed clean wounds without any purulent secretion, and the degree of swelling was less than that in the

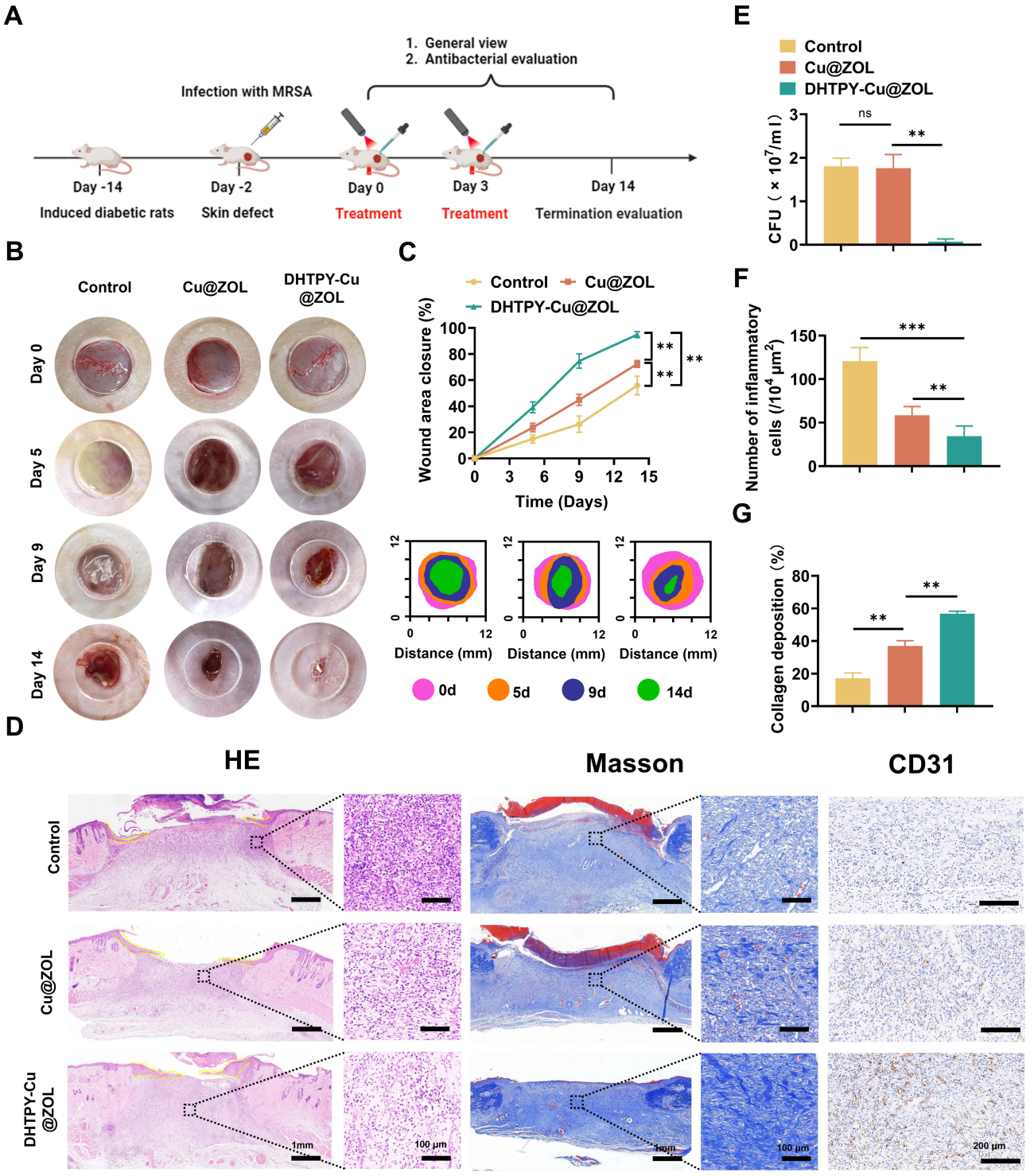

Figure 5 DHTPY-Cu@ZOL's effectiveness in enhancing diabetic wound healing and regeneration in vivo (**P < 0.01 and ***P < 0.001, ns represented no significance). (**A**) Diagram depicting the creation of infected diabetic wounds and the subsequent healing process with therapy. (**B** and **C**) Photographic documentation of wound healing progression under various treatment conditions, with statistical analysis of healing rates over time (n = 3). (**D**) Histological sections from day 9 post-treatment, stained with H&E, Masson, and CD31. (**E**) Bacterial colony counts from wound cultures at day 14 post-treatment (n = 3). (**F**) Quantitative analyses of inflammatory cell count (n = 3). (**G**) Quantitative analyses of collagen content (n=3).

Cu@ZOL group, indicating its effective photodynamic action. These results demonstrate the excellent in vivo therapeutic effect of DHTPY-Cu@ZOL in PDT, showing higher efficiency against MRSA and in wound healing. Wound closure was quantified using ImageJ software to determine the wound healing process (Figure 5C). In the control group, the wound healing was the poorest

among the three groups, with a wound area of 34.6 ± 5.11 mm² remaining on the 14th day. Cu@ZOL significantly promoted wound healing ($P < 0.01$), reducing the wound size to 21.7 ± 1.9 mm², while DHTPY-Cu@ZOL mostly induced complete wound closure (4 ± 1.8 mm²), significantly superior to the method of merely consuming H_2O_2 to produce oxygen ($P < 0.01$). H&E staining was utilized to assess bacterial load, the growth of the epithelium and inflammation levels following treatment. Fourteenth day after treatment, wounds treated with PBS (control group) and Cu@ZOL+light (Cu@ZOL group) exhibited a substantial bacterial presence, exceeding 1×10^7 CFU, while DHTPY-Cu@ZOL+Light treatment group (DHTPY-Cu@ZOL group) demonstrated a significant reduction in bacterial counts as shown in Figure 5E.

Ninth day after treatment, H&E staining results indicated noticeable inflammation in control group and Cu@ZOL group. On the contrary, the DHTPY-Cu@ZOL group showed marked alleviation of inflammation, as evidenced in Figure 5D and F. Among the three groups, the almost complete epithelialization was only observed in the DHTPY-Cu@ZOL group at day 14 (Figure S2). Collagen (Col) deposition density, an important criterion for wound healing, was studied through Masson's trichrome staining. Compared to control group treatment, Cu@ZOL ($P < 0.01$) and DHTPY-Cu@ZOL ($P < 0.01$) treatments significantly increased Col density (Figure 5D and G). These in vivo results consistently prove that DHTPY-Cu@ZOL effectively promotes wound closure and thicker Col deposition by combining bacterial killing with tissue regeneration. Additionally, angiogenesis, an important process in wound healing, helps deliver growth factors and nutrients to the wound site. Results from CD31 immunohistochemical staining showed that the DHTPY-Cu@ZOL group highly expressed CD31 positive cells (Figures 5D and S3).

To further explore the level of inflammation at the wound site at 14th day, immunofluorescence staining results revealed a decrease in TNF-α positive cells (Figure 6A and C) and an increase in IL-10 positive cells (Figure 6B and D).

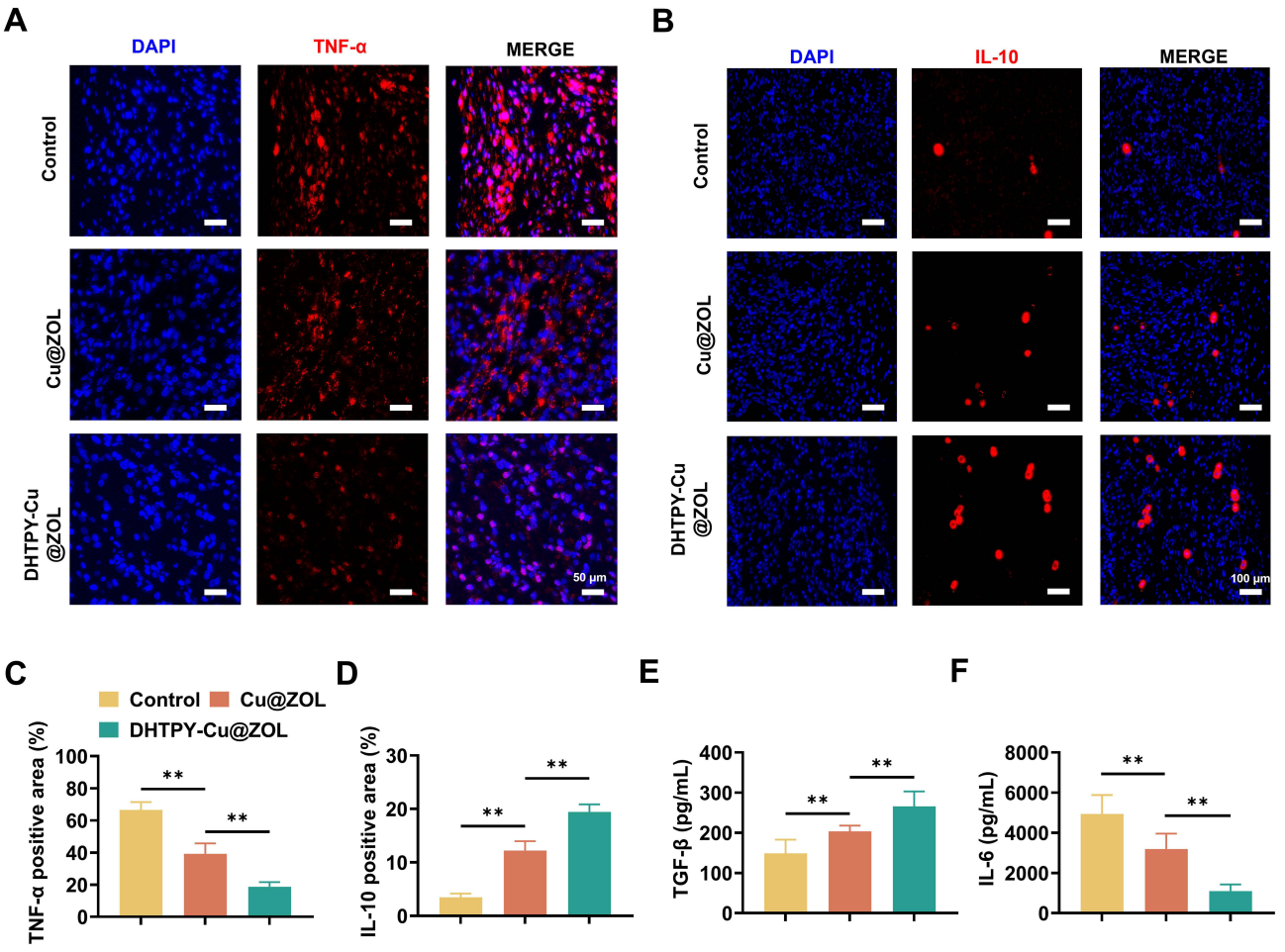

Figure 6 Evaluating the Anti-Inflammatory Impact of DHTPY-Cu@ZOL in Rats (**P < 0.01). (**A**) Confocal microscopy images showcasing TNF-α (red) expression in wound tissues from different treatment groups on day 14. (**B**) Confocal microscopy images showcasing IL-10 (red) expression in wound tissues from different treatment groups on day 14. (**C**) Quantitative fluorescence analyses of TNF-α positive area in the wound tissue (n = 3). (**D**) Quantitative fluorescence analyses of IL-10 positive area in the wound tissue (n = 3). (**E**) The levels of TGF-β in the wound tissue were quantified using ELISA on day 14 (n = 3). (**F**) The levels of IL-6 in the wound tissue were quantified using ELISA on day 14 (n = 3).

Subsequently, an enzyme-linked immunosorbent assay (ELISA) was conducted to quantify the concentration of secreted pro-inflammatory and anti-inflammatory cytokines. As expected, the secretion of transforming growth factor-beta (TGF-β) and interleukin-6 (IL-6) was promoted in cells treated with DHTPY-Cu@ZOL (Figure 6E and F), demonstrating their anti-inflammatory capabilities. The above results highlight that through DHTPY-Cu@ZOL treatment-mediated bacterial elimination, inflammation relief, and immune regulation cascade, high-quality healing of chronic wound infections caused by MRSA can be achieved.

In vivo Biocompatibility of DHTPY-Cu@ZOL

To further assess in vivo compatibility, no adverse side effects were observed in rats treated with DHTPY-Cu@ZOL throughout the entire study. The long-term effects of DHTPY-Cu@ZOL were evaluated by monitoring the histopathology and blood chemistry indicators of major organ tissues in both healthy and treated rats, to reveal its biocompatibility in vivo on the 14th day. No necrosis, congestion, or hemorrhage were observed in the heart, liver, spleen, lungs, and kidneys (Figure 7A). Furthermore, through complete blood cell counts and monitoring of various other blood parameters, all results were found to fall within normal ranges (Figure 7B–D). No significant differences were observed in tissue sections of the control and DHTPY-Cu@ZOL

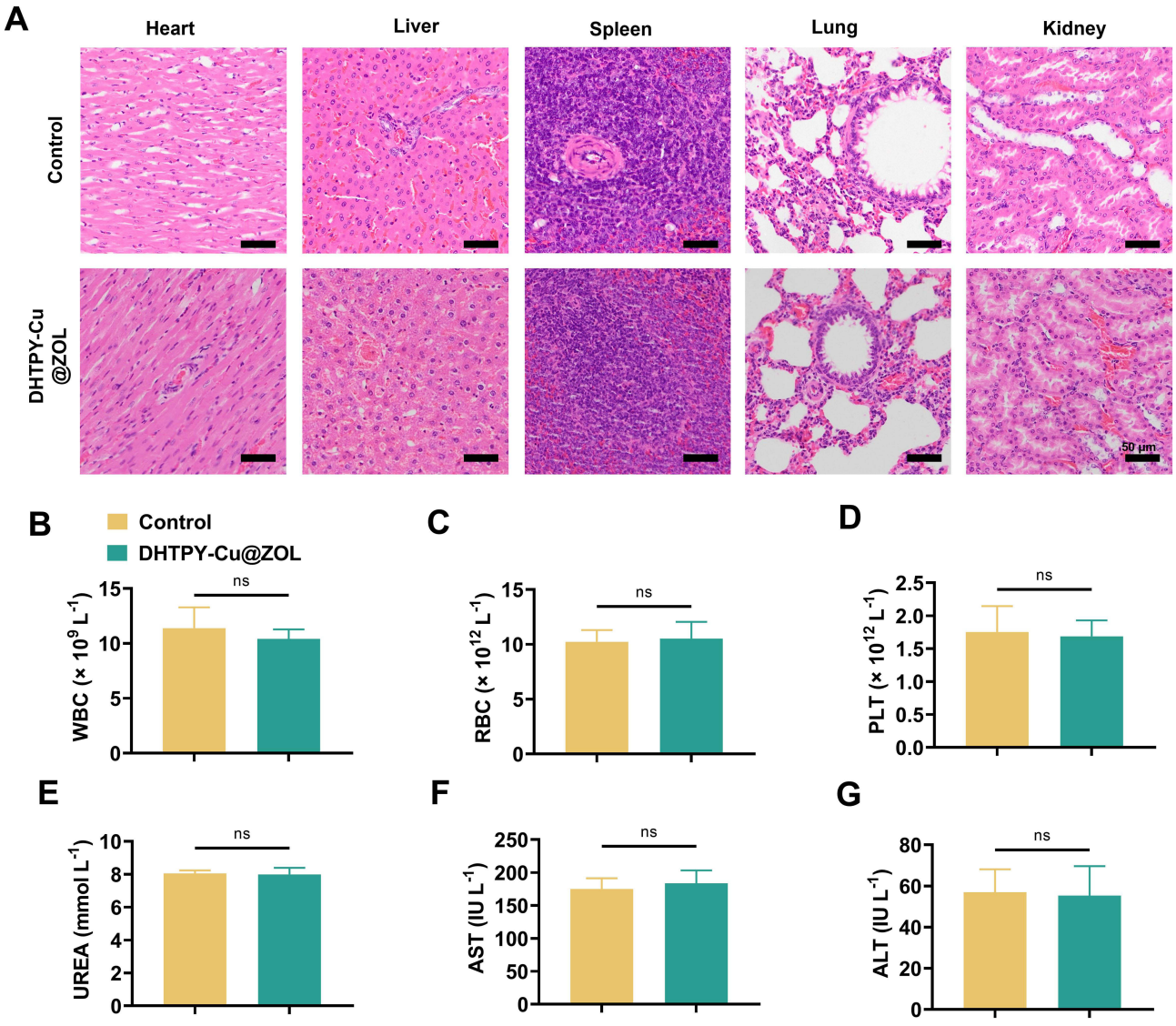

Figure 7 Assessing the biocompatibility of DHTPY-Cu@ZOL (ns represented no significance). (**A**) Analysis of in vivo toxicity in key organs (heart, liver, spleen, lung, and kidney) at 14 days post-treatment. (**B**–**D**) Comparative blood parameter analysis between untreated rats and those treated with various formulations over a 14-day period (n = 3). (**E**) Evaluation of serum renal function indicators (n = 3). (**F** and **G**) Assessment of liver function through serum levels of ALT and AST (n = 3).

treatment groups. Additionally, it is important to measure renal and liver function following continuous administration of DHTPY-Cu@ZOL. The serum renal function indicators, blood urea nitrogen, as well as serum liver function indicators, aspartate aminotransferase (AST) and alanine aminotransferase (ALT) levels in the DHTPY-Cu@ZOL treatment group, were almost similar to those in the control group ($P > 0.05$) (Figure 7E–G). In summary, based on the in vivo results, it can be reasonably hypothesized that DHTPY-Cu@ZOL is an almost non-toxic biocompatible biomaterial, potentially expandable for future applications in numerous biological fields. These findings hold promise for the clinical treatment of chronic wounds and may fulfill unmet clinical needs.

Conclusion

In this study, we confront the challenge of drug-resistant bacterial infections by developing DHTPY-Cu@ZOL nanozyme particles, integrating AIE-type photosensitizers with Cu@ZOL nanozymes. These particles are adept at generating oxygen in the hypoxic conditions common in chronic bacterial infections, thereby overcoming a key limitation of PDT that is highly dependent on oxygen. The copper nanozymes within the particles serve a dual role: they catalyze the decomposition of H_2O_2 into oxygen, alleviating hypoxia, and regulate ROS production to prevent excessive oxidative stress. This enhancement in oxygen availability significantly boosts the efficiency of PDT, ensuring an adequate supply of molecular oxygen for effective ROS generation. The biocompatibility and stability of DHTPY-Cu@ZOL, coupled with their improved PDT efficacy, position them as a promising candidate for clinical applications. This novel approach signifies a significant advancement in non-antibiotic treatments, offering the potential to revolutionize the management of chronic infections caused by drug-resistant bacteria and highlighting the potential of nanozyme-based therapies in overcoming traditional PDT limitations in persistent bacterial infections. DHTPY-Cu@ZOL, as a multifunctional nanomaterial, holds broad prospects for application in the biomedical field. Besides the photodynamic therapy for antibiotic-resistant bacterial infections confirmed in this paper, DHTPY-Cu@ZOL also has potential applications in several other areas such as cancer therapy, bone tissue repair, antimicrobial coatings and so on. Based on the oxygen-enhanced photodynamic therapy principle of DHTPY-Cu@ZOL, it could be used for treating hypoxic solid tumors, especially those that are resistant or hard to treat. Besides, copper-based nanozymes have been proven to stimulate osteoblast proliferation, differentiation, and angiogenesis. DHTPY-Cu@ZOL shows promise for accelerating bone defect repair and osseointegration. DHTPY-Cu@ZOL also could be applied as a coating on the surfaces of medical implants, such as catheters and stents, serving to prevent and control postoperative infections. In summary, DHTPY-Cu@ZOL is poised to become a versatile nanoplatform that plays a significant role in the fields of anti-infection, tissue repair, and regeneration in biomedical engineering.

Ethical Statement

All animal experimentations were approved by the Institutional Animal Care and Ethics Committee of the affiliated Nanhua hospital, University of South China (Approval ID: 2022-ky-164) and performed in accordance with the principles and procedures of the National Institutes of Health (NIH) Guide for the Care and Use of Laboratory Animals and the Guidelines for Animal Treatment of University of South China.

Acknowledgments

This work was funded by the National Natural Science Foundation of China (No. 81772315, 81974328), the Hunan Provincial Science and Technology Department (No. 2021SK4030), the Major Special Project of Hunan Provincial Health and Family Planning Commission (No. 20201906), the Fund Project of Hengyang Science and Technology Innovation Plan (No. 202330046272), the "From 0 to 1" Innovative Research Program (Science, Technology and Medicine) of Sichuan University (No. 2023SCUH0037), the Guangdong Science Foundation for Distinguished Young Scholars (No. 2022B1515020044), the Health Research Project of Hunan Provincial Health Commission (No. W20243047).

Disclosure

The authors report no conflicts of interest in this work.

References

1. Verma R, Verma SK, Rakesh KP, et al. Pyrazole-based analogs as potential antibacterial agents against methicillin-resistance staphylococcus aureus (MRSA) and its SAR elucidation. *Eur J Med Chem*. 2021;212:113134. doi:10.1016/j.ejmech.2020.113134
2. Drougka E, Foka A, Liakopoulos A, et al. A 12-year survey of methicillin-resistant Staphylococcus aureus infections in Greece: ST80-IV epidemic? *Clin Microbiol Infect*. 2014;20(11):O796–803. doi:10.1111/1469-0691.12624
3. Hobley L, Harkins C, MacPhee CE, Stanley-Wall NR. Giving structure to the biofilm matrix: an overview of individual strategies and emerging common themes. *FEMS Microbiol Rev*. 2015;39(5):649–669. doi:10.1093/femsre/fuv015
4. Arnaouteli S, Matoz-Fernandez DA, Porter M, et al. Pulcherrimin formation controls growth arrest of the Bacillus subtilis biofilm. *Proc Natl Acad Sci U S A*. 2019;116(27):13553–13562. doi:10.1073/pnas.1903982116
5. Ciofu O, Moser C, Jensen P, Høiby N. Tolerance and resistance of microbial biofilms. *Nat Rev Microbiol*. 2022;20(10):621–635. doi:10.1038/s41579-022-00682-4
6. Khalid SJ, Ain Q, Khan SJ, et al. Targeting Acyl Homoserine Lactones (AHLs) by the quorum quenching bacterial strains to control biofilm formation in Pseudomonas aeruginosa. *Saudi J Biol Sci*. 2022;29(3):1673–1682. doi:10.1016/j.sjbs.2021.10.064
7. Sherrard LJ, Tunney MM, Elborn JS. Antimicrobial resistance in the respiratory microbiota of people with cystic fibrosis. *Lancet*. 2014;384:9944):703–713. doi:10.1016/s0140-6736(14)61137-5
8. Songca SP, Adjei Y. Applications of antimicrobial photodynamic therapy against bacterial biofilms. *Int J Mol Sci*. 2022;23(6):3209. doi:10.3390/ijms23063209
9. Correia JH, Rodrigues JA, Pimenta S, Dong T, Yang Z. Photodynamic therapy review: principles, photosensitizers, applications, and future directions. *Pharmaceutics*. 2021;13(9):1332. doi:10.3390/pharmaceutics13091332
10. Jia Q, Song Q, Li P, Huang W. Rejuvenated photodynamic therapy for bacterial infections. *Adv Healthc Mater*. 2019;8(14):e1900608. doi:10.1002/adhm.201900608
11. Duo Y, Luo G, Zhang W, et al. Noncancerous disease-targeting AIEgens. *Chem Soc Rev*. 2023;52(3):1024–1067. doi:10.1039/d2cs00610c
12. Li D, Liu P, Tan Y, et al. Type I photosensitizers based on aggregation-induced emission: a rising star in photodynamic therapy. *Biosensors*. 2022;12(9):722. doi:10.3390/bios12090722
13. Liu C, Wang X, Liu J, et al. Near-Infrared AIE dots with chemiluminescence for deep-tissue imaging. *Adv Mater*. 2020;2020:1. doi:10.1002/adma.202004685
14. Xu R, Zhang P, Shen Q, et al. AIE nanocrystals: emerging nanolights with ultra-high brightness for biological application. *Coord Chem Rev*. 2023;477:214944. doi:10.1016/j.ccr.2022.214944
15. Gu X, Tang BZ. No UV irradiation needed! chemiexcited AIE dots for cancer theranostics. *Chem*. 2017;3(6):922–924. doi:10.1016/j.chempr.2017.11.013
16. Chen J, Fan T, Xie Z, et al. Advances in nanomaterials for photodynamic therapy applications: status and challenges. *Biomaterials*. 2020;237:119827. doi:10.1016/j.biomaterials.2020.119827
17. Raza A, Hayat U, Rasheed T, Bilal M, Iqbal HMN. "Smart" materials-based near-infrared light-responsive drug delivery systems for cancer treatment: a review. *J Mater Res Technol*. 2019;8(1):1497–1509. doi:10.1016/j.jmrt.2018.03.007
18. Chen K, He P, Wang Z, Tang BZ. A feasible strategy of fabricating type I photosensitizer for photodynamic therapy in cancer cells and pathogens. *ACS Nano*. 2021;15(4):7735–7743. doi:10.1021/acsnano.1c01577
19. Chen D, Xu Q, Wang W, Shao J, Huang W, Dong X. Type I photosensitizers revitalizing photodynamic oncotherapy. *Small*. 2021;17(31):e2006742. doi:10.1002/smll.202006742
20. Mou X, Wu Q, Zhang Z, et al. Nanozymes for regenerative medicine. *Small Methods*. 2022;6(11):e2200997. doi:10.1002/smtd.202200997
21. Sahu A, Jeon J, Lee MS, Yang HS, Tae G. Antioxidant and anti-inflammatory activities of Prussian blue nanozyme promotes full-thickness skin wound healing. *Mater Sci Eng C Mater Biol Appl*. 2021;119:111596. doi:10.1016/j.msec.2020.111596
22. Hu M, Korschelt K, Daniel P, Landfester K, Tremel W, Bannwarth MB. Fibrous nanozyme dressings with catalase-like activity for H(2)O(2) reduction to promote wound healing. *ACS Appl Mater Interfaces*. 2017;9(43):38024–38031. doi:10.1021/acsami.7b12212
23. Liu L, Wang C, Li Y, et al. Manganese dioxide nanozyme for reactive oxygen therapy of bacterial infection and wound healing. *Biomater Sci*. 2021;9(17):5965–5976. doi:10.1039/d1bm00683e
24. Yang Y, Wu X, Ma L, et al. Bioinspired spiky peroxidase-mimics for localized bacterial capture and synergistic catalytic sterilization. *Adv Mater*. 2021;33(8):e2005477. doi:10.1002/adma.202005477
25. Liang M, Yan X. Nanozymes: from new concepts, mechanisms, and standards to applications. *Acc Chem Res*. 2019;52(8):2190–2200. doi:10.1021/acs.accounts.9b00140
26. Kandathil V, Patil SA. Single-atom nanozymes and environmental catalysis: a perspective. *Adv Colloid Interface Sci*. 2021;294:102485. doi:10.1016/j.cis.2021.102485
27. Yu X, Wang Y, Zhang J, Liu J, Wang A, Ding L. Recent development of copper-based nanozymes for biomedical applications. *Adv Healthc Mater*. 2023;13:e2302023. doi:10.1002/adhm.202302023
28. Liang S, Deng X, Chang Y, et al. Intelligent Hollow Pt-CuS janus architecture for synergistic catalysis-enhanced sonodynamic and photothermal cancer therapy. *Nano Lett*. 2019;19(6):4134–4145. doi:10.1021/acs.nanolett.9b01595
29. Chang M, Hou Z, Wang M, et al. Cu(2) MoS(4) /Au heterostructures with enhanced catalase-like activity and photoconversion efficiency for primary/metastatic tumors eradication by phototherapy-induced immunotherapy. *Small*. 2020;16(14):e1907146. doi:10.1002/smll.201907146
30. Pu Y, Chen S, Yang Y, Mao X. Copper-based biological alloys and nanocomposites for enzymatic catalysis and sensing applications. *Nanoscale*. 2023;15(28):11801–11812. doi:10.1039/d3nr01638b
31. Huang W, Xu P, Fu X, et al. Functional molecule-mediated assembled copper nanozymes for diabetic wound healing. *J Nanobiotechnology*. 2023;21(1):294. doi:10.1186/s12951-023-02048-1
32. Li M, Xie Y, Lei L, Huang H, Li Y. Colorimetric logic gate for protamine and trypsin based on the Bpy-Cu nanozyme with laccase-like activity. *Sensors and Actuat B Chem*. 2022;357:131429. doi:10.1016/j.snb.2022.131429
33. Xi J, Wei G, An L, et al. Copper/carbon hybrid nanozyme: tuning catalytic activity by the copper state for antibacterial therapy. *Nano Lett*. 2019;19(11):7645–7654. doi:10.1021/acs.nanolett.9b02242

34. Liu T, Xiao B, Xiang F, et al. Ultrasmall copper-based nanoparticles for reactive oxygen species scavenging and alleviation of inflammation related diseases. *Nat Commun*. 2020;11(1):2788. doi:10.1038/s41467-020-16544-7
35. Yan H, Wang Y, Huo F, Yin C. Fast-specific fluorescent probes to visualize norepinephrine signaling pathways and its flux in the epileptic mice brain. *J Am Chem Soc*. 2023;145(5):3229–3237. doi:10.1021/jacs.2c13223
36. Fu X, Yu X, Jiang J, et al. Small molecule-assisted assembly of multifunctional ceria nanozymes for synergistic treatment of atherosclerosis. *Nat Commun*. 2022;13(1):6528. doi:10.1038/s41467-022-34248-y
37. Huang X, Zhang W, Peng Y, et al. A multifunctional layered nickel silicate nanogenerator of synchronous oxygen self-supply and superoxide radical generation for hypoxic tumor therapy. *ACS Nano*. 2022;16(1):974–983. doi:10.1021/acsnano.1c08580
38. Zhang J, Jia Q, Yue Z, et al. An electroluminodynamic flexible device for highly efficient eradication of drug-resistant bacteria. *Adv Mater*. 2022;34(17):e2200334. doi:10.1002/adma.202200334
39. Shao Z, Yin T, Jiang J, He Y, Xiang T, Zhou S. Wound microenvironment self-adaptive hydrogel with efficient angiogenesis for promoting diabetic wound healing. *Bioact Mater*. 2022;20:561–573. doi:10.1016/j.bioactmat.2022.06.018
40. Xiong Y, Lin Z, Bu P, et al. A whole-course-repair system based on neurogenesis-angiogenesis crosstalk and macrophage reprogramming promotes diabetic wound healing. *Adv Mater*. 2023;35(19):e2212300. doi:10.1002/adma.202212300